

Figure 4 The 'phase diagram' for the peak effect. Phase coexistence occurs in a large temperature range below the superconducting transition, as sketched in the plot. The data points were measured on a different 2H-NbSe₂ sample (5 × 2 × 0.12 mm), with a static Hall sensor (see text) positioned ~10 μm above the sample surface. The peak effect is observed down to $B \approx 20$ G; for lower fields, a disordered phase persists presumably in the entire temperature range below T_c .

In a range of a.c. fields of 10–30 mG, the position and width of the peak do not depend on the a.c. field amplitude. However, the fine details of the local phase transformation do. Also, on several occasions, for a small a.c. field amplitude of ~5 mG, no peak effect was observed, suggesting that a supercooled disordered phase can be stabilized by the local disorder. In the opposite case of a large a.c. field amplitude of 40 mG, the magnitude of the peak effect decreases, suggesting that a superheated ordered phase can be stabilized by the drive.

Additionally, we speculate that the interface is driven by the change in the circulating shielding current that flows when the field or temperature is changed. The origin of the shielding current is in the equilibrium diamagnetism of the superconductor, including a possible step change in it due to a first-order phase transition^{10,11}. A jump in local induction¹¹ associated with the first-order phase transition could potentially create a current density at least an order of magnitude larger than the shielding a.c. current. The flow of current is then self-balanced between the two phases, and its confinement within the sample geometry determines the overall spatial phase distribution. In a similar fashion to the first-order melting transition in high-temperature superconductors¹², small variations in the pinning strength across the sample may lead to the observed complex shape of the phase boundary.

An important implication of our work is that the two-phase nature of the peak-effect region should be taken into account when producing a coherent explanation of the numerous experimental results. In fact, a consideration of redistribution of current in a two-phase system leads naturally to a simple quantitative model (M.M. *et al.*, manuscript in preparation) of numerous experimentally observed transport anomalies. The two-phase nature of the transition region, as opposed to the commonly considered spatially homogeneous character, is crucial for a proper analysis of the structural data¹³. Also, our result may be relevant to the explanation of the "second peak" phenomenon¹⁴ observed in the high-temperature superconductors.

The peak effect thus appears to be a rare experimental realization of a disorder-driven non-thermal phase transformation in a randomly disordered system. This class of phase transitions is of considerable

present interest, and we hope our results will lead to further theoretical and experimental explorations of the subject. □

Received 29 September; accepted 27 November 2000.

- Pippard, A. B. A possible mechanism for the peak effect in type II superconductors. *Phil. Mag.* **19**, 217–220 (1969).
- Wordenweber, R., Kes, P. H. & Tsuei, C. C. Peak and history effect in two dimensional collective flux pinning. *Phys. Rev. B* **33**, 3172–3180 (1986).
- Bhattacharya, S. & Higgins, M. J. Dynamics of a disordered flux line lattice. *Phys. Rev. Lett.* **70**, 2617–2620 (1993).
- Henderson, W. *et al.* Metastability and glassy behavior of a driven flux line lattice. *Phys. Rev. Lett.* **77**, 2077–2080 (1996).
- Henderson, W., Andrei, E. Y. & Higgins, M. J. Plastic motion of a vortex lattice driven by alternating current. *Phys. Rev. Lett.* **81**, 2352–2355 (1998).
- Banerjee, S. S. *et al.* Disorder, metastability, and history dependence in transformations of a vortex lattice. *Phys. Rev. B* **59**, 6043–6046 (1999).
- Chang, A. M. *et al.* Scanning Hall probe microscopy. *Appl. Phys. Lett.* **61**, 1974–1976 (1992).
- Gilchrist, J. & Konczykowski, M. Superconductor screen viewed as one or two inductive loops. *Physica C* **212**, 43–60 (1993).
- Paltiel, Y. *et al.* Dynamic instabilities and memory effects in vortex matter. *Nature* **403**, 398–401 (2000).
- Zeldov, E. *et al.* Thermodynamic observation of first-order vortex lattice melting transition. *Nature* **375**, 373–376 (1995).
- Ravikumar, G. *et al.* Step change in equilibrium magnetization across the peak effect in 2H-NbSe₂. *Physica C* **322**, 145–150 (1999).
- Soibel, A. *et al.* Imaging the vortex-lattice melting process in the presence of disorder. *Nature* **406**, 282–287 (2000).
- Gammel, P. L. *et al.* Structure and correlation of a flux line lattice in crystalline Nb through peak effect. *Phys. Rev. Lett.* **80**, 833–836 (1998).
- Khaykovich, B. *et al.* Vortex-lattice phase transitions in Bi₂Sr₂CaCu₂O₈ crystals with different oxygen stoichiometry. *Phys. Rev. Lett.* **76**, 2555–2558 (1996).

Acknowledgements

We thank E. Zeldov and E. Andrei for helpful discussions.

Correspondence and requests for materials should be addressed to M.M. (e-mail: marchev@research.nj.nec.com).

An effective gravitational temperature for sedimentation

P. N. Segrè*, F. Liu†, P. Umbanhowar‡ & D. A. Weitz*

* Department of Physics, Harvard University, Cambridge, Massachusetts 02138, USA

† Department of Physics, University of Pennsylvania, Philadelphia, Pennsylvania 19104, USA

‡ Department of Physics and Astronomy, Northwestern University, Evanston, Illinois 60208, USA

The slow sedimentation of suspensions of solid particles in a fluid results in complex phenomena that are poorly understood. For a low volume fraction (ϕ) of particles, long-range hydrodynamic interactions result in surprising spatial correlations¹ in the velocity fluctuations; these are reminiscent of turbulence, even though the Reynolds number is very low^{2–4}. At higher values of ϕ , the behaviour of sedimentation remains unclear; the upward back-flow of fluid becomes increasingly important, while collisions and crowding further complicate inter-particle interactions^{5–8}. Concepts from equilibrium statistical mechanics could in principle be used to describe the fluctuations and thereby provide a unified picture of sedimentation, but one essential ingredient—an effective temperature that provides a mechanism for thermalization—is missing. Here we show that the gravitational energy of fluctuations in particle number can act as an effective temperature. Moreover, we demonstrate that the high- ϕ behaviour is in fact identical to that at low ϕ , provided that the suspension viscosity and sedimentation velocity are scaled appropriately, and that the effects of particle packing are included.

We studied the sedimentation of relatively high concentrations ($0.05 \leq \phi \leq 0.50$) of nearly monodisperse spherical glass beads of mean radii $a = 50 \pm 5 \mu\text{m}$ dispersed in solutions of water and glycerol (viscosity, $\eta \approx 20\text{--}70 \text{ cP}$) that nearly match the refractive index of the particles. Thermally induced brownian motion is negligible compared to gravitational settling, with the Peclet number being $\text{Pe} \approx 10^7$; particle inertia is also negligible, with the particle Reynolds number being $\text{Re} \approx 10^{-4}$. The sample cells were typically 6 cm wide, 0.3 cm deep and 30 cm high, and were placed in a stirred water bath at temperature $T = 23 \pm 1^\circ\text{C}$. The cell was illuminated from behind, and images were collected from the median plane with a CCD (charge-coupled device) camera, using a depth of field of $\sim 0.5\text{--}1 \text{ mm}$. These images were digitized, and velocity profiles were calculated using standard particle-image-velocimetry (PIV) techniques⁹. This yielded two-dimensional velocity maps of 29×39 vectors, each of which is the local average of the velocities of two to four spheres. Initially random dispersions were prepared by vigorously shaking the cell, and measurements were started after the sedimentation front had settled about one-fifth of the cell height, allowing any initial transients to decay. Images were collected from regions of the cell that were far from both the sedimentation front at the top, and the concentrated sediment at the bottom of the cell.

We subtract the mean velocity to focus on velocity fluctuations $\delta\mathbf{V} = \mathbf{V} - V(\phi)\hat{z}$, where $V(\phi)\hat{z}$ is the average settling velocity due to gravity; in Fig. 1 we show typical spatial maps of $\delta\mathbf{V}$ for a sample with $\phi = 0.30$. The magnitudes of the fluctuations are very large, of the order of the average velocity. Moreover, similar to the behaviour at much lower ϕ ¹, the velocity fluctuations are clearly strongly correlated spatially over length scales that are much greater than a . These spatially correlated patterns evolve over time, as illustrated by the sequence of $\delta\mathbf{V}$ maps shown in Fig. 1; it is this complex spatial and temporal pattern which is reminiscent of turbulence (P. M. Chaikin, personal communication and ref 3). Several prominent correlated regions seen in Fig. 1a remain clearly identifiable in Fig. 1b, which is after $\Delta t = 18 \text{ s}$, corresponding to an average settling of $\sim 10a$; however, after $\Delta t = 36 \text{ s}$, corresponding to an average settling of $\sim 20a$, the patterns are nearly completely decorrelated, as shown in Fig. 1c. By examining many such images, we determine the root mean square (r.m.s.) magnitude of the velocity fluctuations, both parallel, ΔV_{\parallel} , and perpendicular, ΔV_{\perp} , to gravity, and plot these as a function of ϕ in Fig. 2. The magnitudes of the r.m.s. fluctuations are comparable to the mean sedimentation velocities, $\Delta V/V(\phi) \approx 1$; thus mixing is substantial during settling. Moreover, $\Delta V/V(\phi)$ is approximately constant for the volume fractions used in this work, $0.05 \leq \phi \leq 0.50$; by contrast, earlier results¹ in very dilute suspensions found a rapid increase for $10^{-4} \leq \phi \leq 0.03$.

The spatial extent of the velocity correlations is quantified by calculating $C_z(z) = \langle \delta V_z(0)\delta V_z(z) \rangle / \Delta V_{\parallel}^2$, where z is parallel to gravity. These correlation functions decay exponentially, as shown in Fig. 3 inset, providing a measure of the characteristic length scale of the correlations of the velocity fluctuations, ξ_{\parallel} . We similarly determine the transverse correlation length in the direction perpendicular to gravity, ξ_{\perp} , for motion parallel to gravity (found from $C_z(x)$, where x is perpendicular to gravity). We plot the ϕ -dependence of both correlation lengths in Fig. 3; both agree well with extrapolations of the behaviour measured for very dilute suspensions, $(\phi \leq 0.03)$ ¹, $\xi_{\perp} \approx 7a\phi^{-1/3}$ and $\xi_{\parallel} \approx 11a\phi^{-1/3}$, as shown by the dashed and dotted lines, respectively. This agreement is surprising because of the significantly different mechanisms influencing particle interactions as ϕ increases; whereas hydrodynamic interactions play a crucial role at all ϕ , short-range lubrication forces, solvent back-flow and excluded-volume effects become increasingly important with increasing ϕ .

We also determine the characteristic timescale over which the velocity fluctuations remain correlated by measuring their temporal correlation at a fixed spatial location that is stationary in the frame of the mean sedimentation velocity,

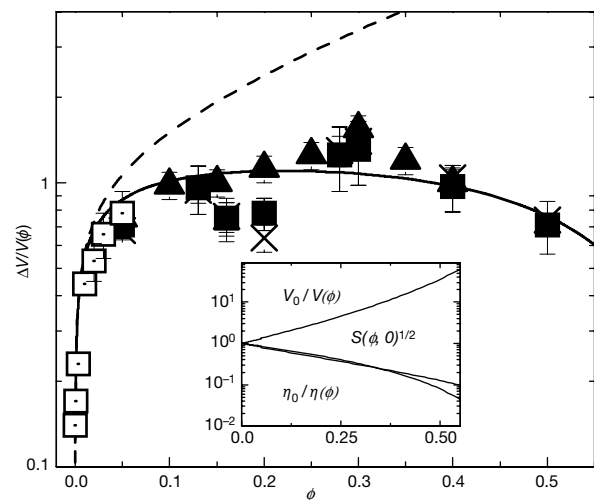


Figure 2 Normalized velocity fluctuations $\Delta V/V(\phi)$ as a function of ϕ . These fluctuations are in the directions parallel (\parallel ; filled squares, this work; triangles, ref. 12; open squares, ref. 1) and perpendicular (\perp ; multiplied by 2, crosses, this work) to gravity. The solid and dashed lines are from equation (2), with $C_0 = 2.6$, with and without $(S(\phi, 0) = 1)$ excluded volume corrections. Inset: ϕ -dependencies of sedimentation velocity, viscosity, and structure factors used in equation (2).

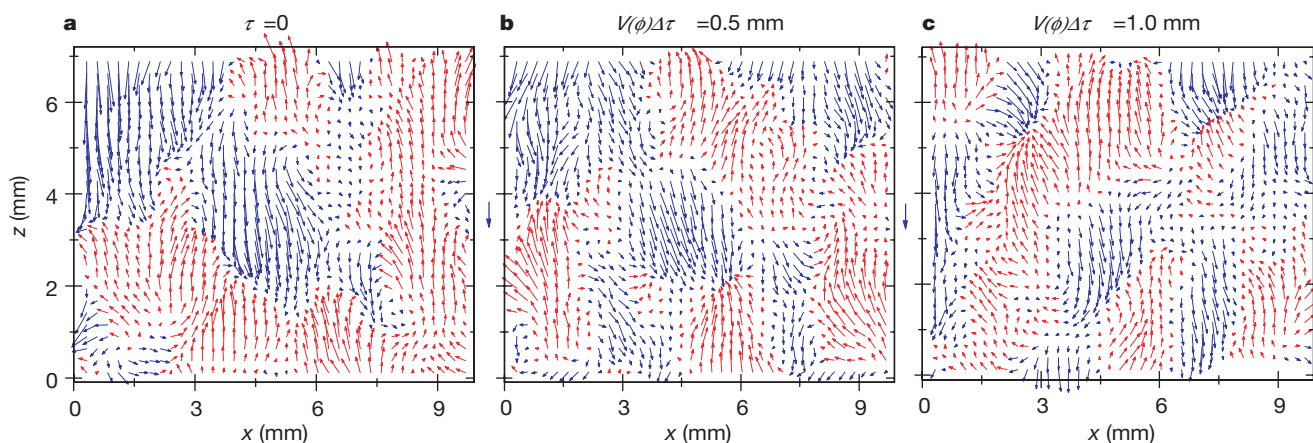


Figure 1 PIV velocity fluctuation ($\delta\mathbf{V} = \mathbf{V} - V(\phi)\hat{z}$) vector maps of a typical sample at $\phi = 0.30$. Data are shown at relative times $t = 0$ (a), $\Delta t = 18 \text{ s}$ (b) and $\Delta t = 36 \text{ s}$ (c). Blue and red colouring is used to distinguish the up and down directions, respectively. The

mean sedimentation velocity, $V(\phi) = 0.028 \text{ mm s}^{-1}$, is represented to scale by the single arrows next to each frame. Each vector represents the local instantaneous velocity of 2–4 particles.

$C(\tau) = \langle \delta V_z(0) \delta V_z(\tau) \rangle / \Delta V^2$. These correlation functions decay exponentially, with a characteristic decay time, τ_d , as shown in Fig. 4 inset. This decay time increases with increasing ϕ , and is comparable to the transit time for a velocity fluctuation, $\tau_\xi = \xi / \Delta V$. Thus, the regions of correlated velocity fluctuations persist long enough that particles within these regions can traverse the correlation length; similar behaviour was observed using ultrasonic scattering from fluidized beds at high ϕ (ref. 10). This suggests a simple physical picture: particles are advected within a correlated velocity fluctuation, travelling a distance of $\sim \xi$ until the correlations decay in a time, τ_d , whereupon the particle becomes entrained in a new region of correlated fluctuating velocity. This behaviour is analogous to a diffusion process, with the mean free path of the diffusion determined by ξ and the mean free time by τ_d . To test this analogy, we compare the diffusion coefficients determined by $D(\phi) = \Delta V^2 \tau_d$ with the self-diffusion coefficients $D_s(\phi)$ measured by tracking tagged particles^{11,12}; as shown in Fig. 4, they are in very good agreement. This establishes a direct relationship between the collective correlations in the velocity fluctuations and the self-diffusion of individual particles.

A simple energy-balance model can be used to relate the magnitude of the velocity fluctuations ΔV to the correlation lengths ξ (refs 1, 6). We assume that the correlations in the velocity fluctuations result from a fluctuation in particle density, of spatial extent ξ , corresponding to a fluctuation in particle mass of Δm_ξ . We determine the magnitude of this fluctuation by balancing the gravitational potential energy gained as this fluctuation moves up or down relative to the background suspension with the energy lost to viscous dissipation due to shear. Thus, for a system in steady state we equate the rate of energy gain, $dE_g/dt = \Delta m_\xi g \Delta V$, with the rate of energy dissipation, $dE_v/dt = (6\pi\eta(\phi)\xi\Delta V)\Delta V$, where $\eta(\phi)$ is the ϕ -dependent viscosity of the suspension. This leads to:

$$\Delta V = \frac{\Delta m_\xi g}{6\pi\eta(\phi)\xi} \quad (1)$$

We assume that mass fluctuations arise from random fluctuations in particle number in a volume of ξ^3 , $\Delta m_\xi = \Delta N_\xi m_1$, where $m_1 = (4\pi/3)a^3\Delta\rho$ is the buoyant mass of a single particle of volume v_p whose density differs from that of the fluid by $\Delta\rho$. The average number of particles in this volume is $\langle N_\xi \rangle = (\xi/a)^3\phi$, which is independent of ϕ , given the measured scaling of ξ . We expect ΔN_ξ

to scale as $\langle N_\xi \rangle^{1/2}$; however, we must also incorporate the effects of excluded volume as ϕ increases, and thus obtain $\Delta N_\xi = [\langle N_\xi \rangle S(\phi, 0)]^{1/2}$, where $S(\phi, 0)$ is the static structure factor in the small wavevector limit¹³. Thus, for the parallel velocity fluctuations, we obtain

$$\frac{\Delta V}{V(\phi)} = C_0 \phi^{1/3} \left[\frac{V_0}{V(\phi)} \frac{\eta_0}{\eta(\phi)} \sqrt{S(\phi, 0)} \right] \quad (2)$$

where $C_0 = \sqrt{11} \approx 3.3$ and $V_0 = (2/9)\Delta\rho g a^2/\eta_0$ is the Stokes settling velocity at infinite dilution in a fluid of viscosity η_0 .

To compare this prediction with our data, we use the measured¹⁴ functional form for the sedimentation velocity, $V(\phi)/V_0 = (1 - \phi)^5$, which is in good agreement with our data. For the viscosity and structure factor, we use expressions for suspensions of brownian hard spheres in thermal equilibrium. We obtain the static structure factor from the isothermal compressibility, $S(\phi, 0) = (k_B T)/\nu_p = [\partial \Pi / \partial \phi]^{-1}$, where we use the Carnahan–Starling equation of state for the osmotic pressure¹³, $\Pi(\phi) = (k_B T/\nu_p)[(\phi + \phi^2 + \phi^3 - \phi^4)/(1 - \phi)^3]$. Since the shear rates generated by the fluctuations, $\dot{\gamma} = \Delta V/\xi$, are much larger than the rate of thermal brownian diffusion, D_B/a^2 , ($Pe = \dot{\gamma}/(D_B/a^2) \approx 10^4$), we obtain the viscosity from the functional form measured in the high-shear-rate, or high-Peclet-number, limit, where brownian effects are negligible and configurational effects dominate^{15,16}, $\eta(\phi)/\eta_0 = (1 - \phi/0.71)^{-2}$. Using the functional forms in equation (2), an excellent agreement is obtained with the measured value of the velocity fluctuations as a function of ϕ , as shown by the solid line in Fig. 2. This agreement is notable especially given the strong ϕ -dependencies of $V(\phi)$, $\eta(\phi)$ and $S(\phi, 0)$, shown in Fig. 2 inset; we note in particular that the effects of volume exclusion are critically important. We emphasize that we use the functional forms for a thermal system to describe an athermal system. However, the main effect of thermalization is to ensure that the system explores phase space; although the thermalization mechanism is different for a sedimenting system as compared to a brownian system, sedimenting particles are still thermalized in that they can explore accessible phase space. Thus the effects of volume exclusion at high ϕ are similar in both cases, allowing us to use these expressions.

As a further test of the consequences of the thermalization, we also calculate the behaviour of the self-diffusion coefficient using

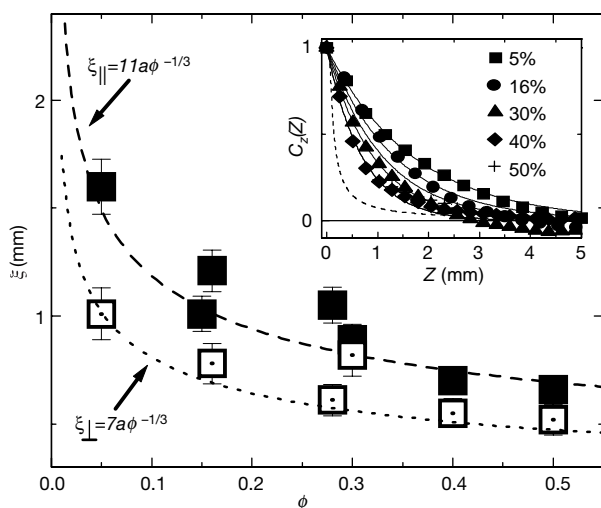


Figure 3 Correlation lengths, ξ , as a function of ϕ . Filled squares, longitudinal correlation lengths, $\xi_{||}$; open squares, transverse correlation lengths, ξ_{\perp} . The dashed lines are extrapolations of the scaling results found at very low ϕ (ref. 1). Inset: longitudinal velocity correlation functions $C_v(z)$ as a function of z , the distance in the direction of gravity. The dashed line is the theoretical result for an isolated sphere of size a , with no cooperative effects¹³.

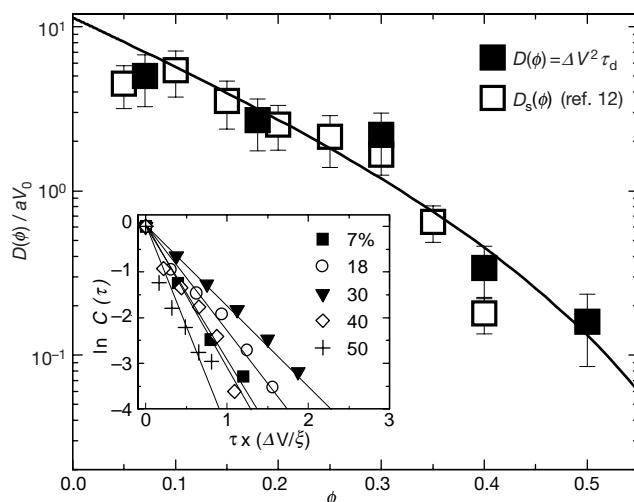


Figure 4 Normalized diffusion coefficients $D(\phi) = \Delta V^2 \tau_d$ from this work and $D_s(\phi)$ from ref. 12. Solid line: $D(\phi) = 11.4aV_0\{\eta_0/[\eta(\phi)]\}[S(\phi, 0)]^{1/2}$. Inset: time correlation functions, $C(\tau)$, of the velocity vector maps plotted as a function of τ normalized by the ϕ -dependent transit time for a velocity fluctuation $\xi/\Delta V$. The decorrelation time τ_d is found from fits to $C(\tau) = \exp(-\tau/\tau_d)$, shown as solid lines, yielding on average $\tau_d \approx \xi/2.5\Delta V$.

$D(\phi) = \Delta V^2 \tau_d$. We approximate the behaviour of the decay time with $\tau_d = \xi/2.5\Delta V$, and use the measured functional form for ξ , and the expression for ΔV in equation (2), thereby obtaining a new analytic expression for the diffusion coefficient, $D(\phi) = 11.4aV_0\{\eta_0/[\eta(\phi)]\}[S(\phi, 0)]^{1/2}$. We again obtain very good agreement with the data, as shown by the solid line in Fig. 4. This agreement further validates our use of thermal equilibrium quantities to describe this highly athermal system.

We can obtain insight into the origin of the thermalization of the sedimenting particles by considering the diffusion coefficient. We take the approximate relation based on our data, $D(\phi) \approx \Delta V\xi/2.5$, and use equation (1) for the velocity fluctuations, to obtain

$$D(\phi) = \frac{C_1 \Delta m_g g \xi}{6\pi\eta(\phi)\xi} \quad (3)$$

where $C_1 \approx 0.4$. This expression has the same functional form as the Stokes–Einstein equation for the diffusion coefficient of thermalized particles. This allows us to identify the effective temperature, $k_B T = C_1 \Delta m_g g \xi$, which provides the equivalent of thermal energy to the system allowing it to explore phase space, and resulting in the diffusive motion of the particles. But, here it is clearly the gravitational energy of the fluctuation in particle density which drives the thermalization. We note that it is only the fluctuating part of the energy, that arising from Δm_g , which drives the system and causes the diffusive motion. By contrast, the full buoyant mass of the particles is much larger, but contributes only to the average settling, and not to the fluctuations which are the origin of the thermalization. The conversion of potential energy into viscous shear energy, rather than translational kinetic energy, is a consequence of the vanishingly small Reynolds number; Re is related to the ratio of kinetic to shear energy.

Finally, we note that the effective temperature can only be defined for the parallel component of the motion; in the perpendicular direction, there is no gravitational potential energy. The difference in the parallel and perpendicular components of the diffusion coefficients suggest that the effective temperature also exhibits an asymmetry¹²; for the perpendicular temperature it must be the coupling of the two components of the velocity fluctuations that causes the thermalization and leads to the diffusive motion. Nevertheless, these results provide a clear measure of the effective temperature for sedimenting particles, and offer new insight into the relationship between the diffusive motion of individual particles and collective correlations of the velocity fluctuations. □

Received 6 October; accepted 30 November 2000.

1. Segrè, P. N., Herbolzheimer, E. & Chaikin, P. M. Long-range correlations in sedimentation. *Phys. Rev. Lett.* **79**, 2574–2577 (1997).
2. Xue, J.-Z., Herbolzheimer, E., Rutgers, M. A., Russel, W. B. & Chaikin, P. M. Diffusion, dispersion, and settling of hard spheres. *Phys. Rev. Lett.* **69**, 1715–1718 (1992).
3. Tong, T. & Ackerson, B. J. Analogies between colloidal sedimentation and turbulent convection at high Prandtl numbers. *Phys. Rev. E* **58**, R6931–R6934 (1998).
4. Levine, A., Ramaswamy, S., Frey, E. & Bruinsma, R. Screened and unscreened phases in sedimenting suspensions. *Phys. Rev. Lett.* **81**, 5944–5947 (1998).
5. Caflisch, R. E. & Luke, J. H. C. Variance in the sedimentation speed of a suspension. *Phys. Fluids* **28**, 759–760 (1985).
6. Hinch, E. J. in *Disorder and Mixing* (eds Guyon, E., Nadal, J.-P. et al. Pomeau, Y.) 153–185 (Kluwer Academic, Dordrecht, 1988).
7. Koch, D. L. & Shaqfeh, E. S. G. Screening in sedimenting suspensions. *J. Fluid Mech.* **224**, 276–303 (1991).
8. Brenner, M. P. Screening mechanisms in sedimentation. *Phys. Fluids* **11**, 754–772 (1999).
9. Adrian, R. J. Particle-imaging techniques for experimental fluid mechanics. *Annu. Rev. Fluid Mech.* **23**, 261–304 (1991).
10. Cowan, M. L., Page, J. H. & Weitz, D. A. Velocity correlations in fluidized suspensions probed by ultrasonic correlation spectroscopy. *Phys. Rev. Lett.* **85**, 453–456 (2000).
11. Nicolai, H. & Guazzelli, E. Effect of the vessel size on the hydrodynamic diffusion of sedimenting spheres. *Phys. Fluids* **7**, 3–5 (1995).
12. Nicolai, H., Herzhaft, B., Hinch, E. J., Oger, L. & Guazzelli, E. Particle velocity fluctuations and hydrodynamic self-diffusion of sedimenting non-Brownian spheres. *Phys. Fluids* **7**, 12–23 (1995).
13. Russel, W. B., Saville, D. A. & Schowalter, W. R. *Colloidal Dispersions* (Cambridge Univ. Press, Cambridge, 1989).

14. Richardson, J. F. & Zaki, W. N. Sedimentation and fluidization I. *Trans. Inst. Chem. Eng.* **32**, 35–53 (1954).
15. de Kruif, C. G., van Iersel, E. M. F., Vrij, A. & Russel, W. B. Hard sphere colloidal dispersions: viscosity as a function of shear rate and volume fraction. *J. Phys. Chem.* **83**, 4717–4725 (1985).
16. Bender, J. W. & Wagner, N. J. Reversible shear thickening in monodisperse and bidisperse colloidal dispersions. *J. Rheol.* **40**, 899–916 (1996).

Acknowledgements

We thank M. Brenner, S. Tee, P. Tong, A. J. C. Ladd, B. J. Ackerson, P. Mucha and A. Levine for discussions. This work was supported by NASA, NSF and the donors of the Petroleum Research Fund, administered by the ACS. Current address of P.N.S. is NASA MSFC, Huntsville, AL 35802 (Phil.Segre@msfc.nasa.gov).

Correspondence and requests for materials should be addressed to D.A.W. (e-mail: weitz@deas.harvard.edu) or P.N.S.

Pumping of nutrients to ocean surface waters by the action of propagating planetary waves

B. Mete Uz, James A. Yoder & Vladimir Osychyn

Graduate School of Oceanography, University of Rhode Island, S. Ferry Road, Narragansett, Rhode Island 02882, USA

Primary productivity in the oceans is limited by the lack of nutrients in surface waters. These nutrients are mostly supplied from nutrient-rich subsurface waters through upwelling and vertical mixing¹, but in the ocean gyres these mechanisms do not fully account for the observed productivity². Recently, the upward pumping of nutrients, through the action of eddies, has been shown to account for the remainder of the primary productivity; however, these were regional studies which focused on mesoscale (100-km-scale) eddies^{3–6}. Here we analyse remotely sensed chlorophyll and sea-surface-height data collected over two years and show that 1,000-km-scale planetary waves, which propagate in a westward direction in the oceans, are associated with about 5 to 20% of the observed variability in chlorophyll concentration (after low-frequency and large-scale variations are removed from the data). Enhanced primary production is the likely explanation for this observation, and if that is the case, propagating disturbances introduce nutrients to surface waters on a global scale—similar to the nutrient pumping that occurs within distinct eddies.

Much of the motion in the open ocean is baroclinic: at the surface, geostrophic flow balances the pressure gradient caused by a sloping sea surface. The geostrophic current is typically strongest near the surface, and decreases with depth. Because the horizontal pressure gradient must similarly decrease with depth in order to maintain geostrophic balance, constant-density surfaces must slope in the opposite direction to the sea surface. As a result, a baroclinic disturbance that displaces the constant-density surfaces upwards has a negative sea surface height (SSH) anomaly, which can be measured by altimeters. These disturbances propagate westward—as planetary waves or eddies—mostly due to the variation of the Coriolis parameter with latitude. Westward-propagating first-mode baroclinic features dominate the propagating components of the SSH satellite-sensed record from the TOPEX/POSEIDON mission^{7–9}. They have also been observed in images of sea surface temperature from the satellite-borne Advanced Very High Resolution Radiometer^{10–12}.

If the displacement of constant-density surfaces by baroclinic disturbances brought new nutrients into the euphotic zone, the concentration of phytoplankton chlorophyll would be expected to